Magnonic Band Structure in Vertical Meander-Shaped $Co_{40}Fe_{40}B_{20}$ Thin Films

Gianluca Gubbiotti,[1,*] Alexandr Sadovnikov,[2] Evgeny Beginin,[2] Sergey Nikitov,[2,3,4] Danny Wan,[5] Anshul Gupta,[5] Shreya Kundu,[5] Giacomo Talmelli,[5,6] Robert Carpenter,[5] Inge Asselberghs,[5] Iuliana P. Radu,[5] Christoph Adelmann,[5] and Florin Ciubotaru[5]

[1] *Istituto Officina dei Materiali del CNR (CNR-IOM), Sede Secondaria di Perugia, c/o Dipartimento di Fisica e Geologia, Università di Perugia, I-06123 Perugia, Italy*

[2] *Laboratory Magnetic Metamaterials, Saratov State University, 83 Astrakhanskaya Street, Saratov 410012, Russia*

[3] *Kotel'nikov Institute of Radioengineering and Electronics, Russian Academy of Sciences, Moscow 125009, Russia*

[4] *Terahertz Spintronics Laboratory, Moscow Institute of Physics and Technology (National University), 9 Institutskii Lane, Dolgoprudny, 141700, Russia*

[5] *Imec, 3001 Leuven, Belgium*

[6] *Departement Materiaalkunde, KU Leuven, 3001 Leuven, Belgium*

(Received 14 August 2020; accepted 12 November 2020; published 29 January 2021)

Exploring the third dimension in magnonic systems is essential for the investigation of alternative physical phenomena and for the control of spin-wave propagation at the nanoscale. Here, the characteristics of spin waves in vertical meander-shaped $Co_{40}Fe_{40}B_{20}$ thin films consisting of nanosegments located at 90° angles with respect to each other are investigated by Brillouin-light-scattering spectroscopy over four Brillouin zones in reciprocal space. We reveal the dispersion relations and the periodic character of several dispersive branches as well as alternating frequency bands, where spin waves are allowed or forbidden to propagate. Between each couple of successive modes, frequency band gaps exist only for wave numbers $k = 2m\pi/a$, where m is an integer number and a is the size of the meander unit cell, whereas the spectra show propagating modes in the orthogonal film segments for all the other wave numbers. Micromagnetic simulations and analytical calculations are used to understand and explain the results in terms of the mode spatial localization and symmetry. We show that the width and the center frequency of the magnonic band gaps can be controlled by changing the geometrical parameters of the meander-shaped film. The investigated samples behave as three-dimensional waveguides where spin waves propagate in the film segments located at 90° angles with respect to each other, thus making possible vertical spin-wave transport for multilayer magnonic architectures and signal processing.

DOI: 10.1103/PhysRevApplied.15.014061

I. INTRODUCTION

The concept of magnonic crystals (MCs), magnetic metamaterials with periodically modulated properties on the nanoscale, was proposed about 20 years ago as the magnetic counterpart of photonic crystals [1–3]. MCs exhibit engineered and reprogrammable spin-wave (SW) b and structures with alternating frequency gaps and allowed bands for SW propagation [4,5]. MCs with periodicity in one and two dimensions have been widely studied in various arrangements [6–16] and have played a central role in the research field of magnonics, which addresses the use of SWs, or magnons (the SW quanta), as a tool for signal processing, communication and computation with promising prospects for low energy consumption and potential compatibility with the next generation of beyond CMOS electronic circuits [17–20].

In recent years, in order to explore new physical effects and functionalities, increasing attention has been given to structures that are periodic in the film plane but inhomogeneous along the perpendicular direction [21–23]. The inhomogeneity along the out-of-plane direction significantly influences the SW propagation in the periodic landscape of the planar ferromagnetic film. For example, the vertical stacking of ferromagnetic materials offers more coupling mechanisms, i.e., an interplay between dipolar and interlayer exchange due to small interlayer separation whereas in two-dimensional (2D) systems the coupling is essentially based on the long-range dipolar interaction. Single and coupled waveguides were considered only in the planar configuration, e.g., directional couplers performing the functions of a waveguide crossing element and frequency-selective magnonic drop filters in complex

*gubbiotti@iom.cnr.it

magnonic circuitry [24–26]. The interest in vertically coupled magnetic structures follows a similar trend in CMOS electronics [27,28], where it enables a transition from two-dimensional to three-dimensional (3D) architectures and also provides a possible roadmap for further scaling [29,30]. The advantages of 3D over 2D magnetic systems are also related to the different areas of research, physical effects, and potential applications [31,32]. For example, one can explore unidirectional SW propagation, indirect band gaps [33], or curvature-induced alternative dynamic effects [34]. From the applications point of view, 3D integration permits more functionality in a smaller space, thereby allowing for a larger number of vertical interconnections between the layers and an increased element density in scalable and reconfigurable magnonic networks.

In this work, we propose MCs fabricated into nanometrically thick vertical meander-shaped $Co_{40}Fe_{40}B_{20}$ (CoFeB) films consisting of ferromagnetic nanoscale segments located at 90° angles with respect to each other, allowing for SW propagation in three dimensions without significant losses in the junction region. This approach avoids the limitations of SW manipulation and steering [35,36], which are hard to realize using in-plane magnetized films due to the anisotropic SW dispersion that depends on the relative orientation between the magnetization and the wave vector. The magnonic band structure, measured by wavevector-resolved Brillouin-light-scattering (BLS) spectroscopy [37], exhibits full band gaps (BGs), whose width and center frequency depend on the CoFeB film thickness. Micromagnetic simulations accurately reproduce the experimental dispersion and the simulated mode profiles reveal the presence of extended and quantized standing SW modes in the horizontal and vertical segments. Finally, the formation of the magnonic band gaps as well as the dependence of their width and center frequency on the geometric film parameters are explained by theoretical calculations performed using the transfer matrix method (TMM).

The vertical meander-shaped ferromagnetic films with nanometric thickness can be considered as a prototype of 3D integrated magnonic structures that permit the vertical shifting of propagating SW from one layer to another placed at different heights. This opens up the prospect of increasing the density of magnonic elements for scalable networks and the realization of the multilevel architectures of SW signal processing.

II. SAMPLE FABRICATION

Magnetic $Co_{40}Fe_{40}B_{20}$ meander-shaped films are processed on Si wafers using an industrial 300-mm platform. In a first step, a 250-nm-thick SiO_2 is formed by controlled thermal oxidation of the Si substrate. The SiO_2 is then patterned to form a periodic meanderlike surface using 248-nm-DUV lithography and conventional reactive-ion etching chemistry. The resulting periodic grating has a height of $h = 50$ nm and a width of 300 nm. Subsequently, Ta(2 nm)/CoFeB/Ta(2 nm) films are grown by physical vapor deposition on top of the grating. The Ta serves as a seed and cap layer to prevent the oxidation of the magnetic CoFeB films. The array lattice constant is $a = 600$ nm resulting in an edge of the Brillouin zone (BZ) in reciprocal space equal to $\pi/a = 0.52 \times 10^7$ rad/m.

Two samples with different thicknesses (d_1) and widths (d_2) of the CoFeB horizontal and vertical nanosegments, respectively, are fabricated. A schematic drawing of the meander-shaped film is shown in Fig. 1(a). The geometric parameters for the first sample are $d_1 = 23$ nm and $d_2 = 12$ nm whereas for the second sample $d_1 = 15$ nm and $d_2 = 8$ nm. In the remaining part of the paper, these samples are labeled as d_1-d_2, i.e., 23-12 and 15-8 samples, respectively. The meander lattice constant a is kept constant for both samples. SEM images of the 23-12 meander-shaped CoFeB film are depicted in Figs. 1(b) and 1(c). It can clearly be seen that the CoFeB film coats the Si grating, as well as well-defined vertical segments of nearly 90° angles.

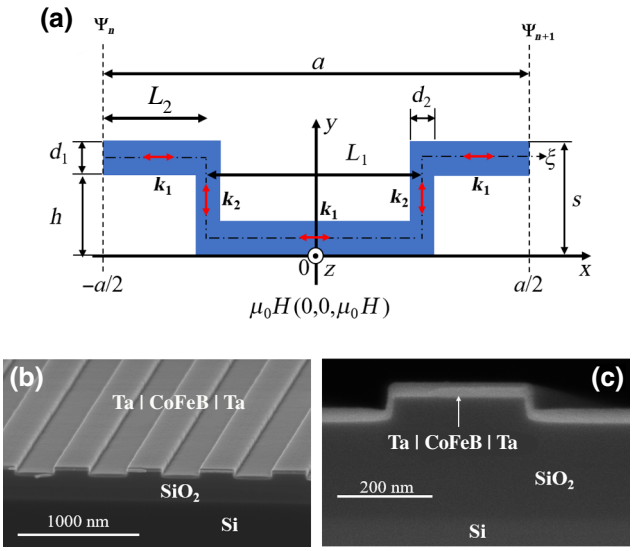

FIG. 1. (a) Cross-section sketch of the meander-shaped film unit cell with a periodicity of $a = L_1 + 2L_2 = 600$ nm, where L_1 and L_2 are the lengths of the horizontal nanosegments with thickness d_1. The width of the vertical segments is d_2, the meander depth is $h = 50$ nm, and the total meander thickness is thus $S = h + d_1$. The dashed-dotted line represents the coordinate (ξ) along the meander structure. An external magnetic field is applied along the z direction and propagation occurs in the x-y plane. k_1 and k_2 represent the SW wave numbers along the horizontal and vertical segments, respectively. Ψ_n and Ψ_{n+1} are the SW amplitudes at the input ($x = -a/2$) and output ($x = +a/2$) sections of the meander-structure unit cell. (b), (c) SEM images of the meander-shaped 23-12 CoFeB film.

Hysteresis loops of the meander-shaped and plane CoFeB films are measured at room temperature by the MOKE in the longitudinal configuration, using a photoelastic modulator operating at 50 kHz and lock-in amplification. The applied magnetic field (H), directed along z direction,is swept from $+30$ mT to -30 mT. Measured loops for the meander-shaped films are square with 100% remanence and coercivities of about 6 and 8 mT for the 23-12 and 15-8 samples, respectively, as shown in Fig. S1 within the Supplemental Material [38].

III. SPIN-WAVE SPECTRA MEASURED BY BRILLOUIN-LIGHT-SCATTERING SPECTROSCOPY

BLS spectra from thermally excited SWs are measured in the 180° backscattering geometry using a 200-mW solid-state laser operating at a wavelength $\lambda = 532$ nm. The light is focused on the sample by a camera objective with a numerical aperture of 0.24, resulting in a laser spot diameter of about 30 to 40 μm. The frequency of the scattered light is analyzed using a $(3+3)$-tandem Fabry-Perot interferometer [39]. Since light scattered from SWs has a polarization rotated by 90° with respect to the incident beam, an analyzer set at extinction suppresses the signal from both elastically scattered and surface phonon-scattered light.

The sample is mounted on a goniometer, which allows us to choose a specified angle of incidence of the light (θ) with an accuracy of 1°. Due to conservation of the in-plane momentum, by changing θ it is possible to select the magnitude of the in-plane component of the SW wave vector [$k = (4\pi/\lambda)\sin(\theta)$]. To measure the SW dispersion (frequency versus k) and to map the magnonic band structure, the magnon wavevectors k are swept along the x direction from zero to the edge of the fourth Brillouin zone at $4\pi/a = 2.08 \times 10^7$ rad/m. An external magnetic field of $\mu_0 H = 50$ mT is applied in the sample plane along the z axis, in the so-called magnetostatic-surface-wave (MSSW) configuration. This applied field ensured the saturation of the CoFeB magnetization, as can be inferred from the MOKE loops presented in Fig. S1 within the Supplemental Material [38]. The comparison between the measured and calculated dispersion (frequency versus wave vector) for planar 23-nm and 15-nm-thick CoFeB films is shown in Fig. S2 within the Supplemental Material [38].

Figure 2 presents the sequence of the BLS spectra for the two investigated samples over the first two BZs, i.e., by varying k from 0 to $2\pi/a = 1.04 \times 10^7$ rad/m, where $a = 600$ nm is the magnonic unit cell. Several well-resolved peaks are observed on both the Stokes and anti-Stokes side of the spectra. The red and blue highlighted peaks correspond to the two lowest-frequency SW modes, which exhibit the largest frequency variation within the investigated wave-vector range. The frequency separation between these two modes decreases from $k = 0$ to $k = \pi/a$ where the two peaks merge and can not be resolved anymore. Upon further increasing k to $k = 2\pi/a$, they split again until they reach the same frequency values measured at $k = 0$. For the 23-12 meander film, the peak at 27.2 GHz, whose frequency is independent on k, corresponds to the first perpendicular-standing spin-wave (PSSW) mode of the 23-nm-thick horizontal segment. It should be noted that the frequency of the PSSW mode for the 15-8 sample is well above 20 GHz and therefore the corresponding peaks are not visible in the BLS spectra.

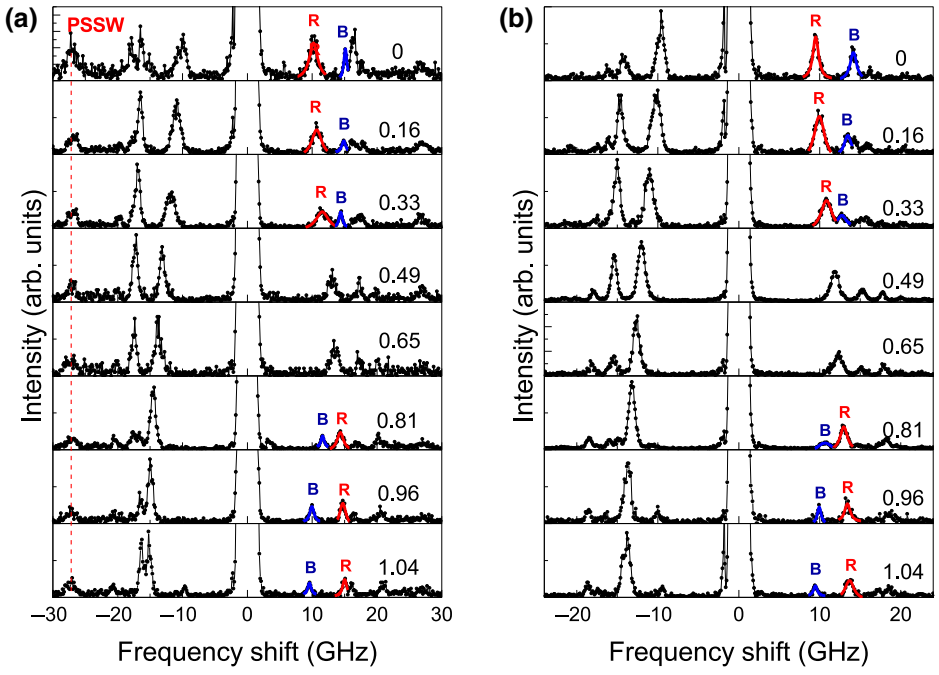

FIG. 2. BLS spectra at $\mu_0 H_0 = 50$ mT recorded at different k values within the first two BZs for (a) 23-12 and (b) 15-8 meander-shaped CoFeB films. Labels of each spectrum correspond to the k value expressed in 10^7 rad/m. On the anti-Stokes side of the spectra, the two lowest frequency modes are highlighted by the red (R) and blue (B) peak. For the 23-12 sample, a vertical dashed line is included as a guide for the eye to indicate the position of the PSSW mode.

IV. MICROMAGNETIC SIMULATIONS OF MAGNONIC BAND STRUCTURE

To model the dynamic response and the magnonic band structure experimentally obtained by Brillouin-light-scattering spectroscopy, we perform micromagnetic simulations using the open-source GPU accelerated MuMax3 software [40]. The computational region of the meander-shaped film is depicted in Fig. 1(a). Along the x and z axes, periodic boundary conditions (PBCs) are established while along the y axis, the size of the region corresponds to the height S of the studied meander structures.

The CoFeB films are discretized into micromagnetic cells of dimensions $\Delta x = \Delta y = \Delta z = 1 \times 1 \times 1$ nm^3. As in experiment, a bias magnetic field of 50 mT is directed along the z axis [see Fig. 1(a)]. To excite SWs in the system, an out-of-plane (y direction) sinc-function magnetic field with an amplitude of 1 mT and with a cut-off frequency of 35 GHz is applied in the excitation region of Fig. S2 within the Supplemental Material [38]. The SW propagation characteristics are obtained by means of a Fourier transform of the temporal evolution of the average magnetization component along the y direction [$M_y(t)$] over a simulation time of 300 ns within the detection region of Fig. S2 within the Supplemental Material [38]. The spatial profile of each mode in one period of the meander structure is extracted by plotting the M_y component of the dynamic magnetization for the frequencies of the SW modes through the continuous-wave excitation regime of the SW signal.

For the magnonic band-structure calculations, the computational structure has dimensions of 8000 and 300 nm along the x and z directions, respectively. To obtain the dispersion characteristics, a computational region containing 10 meander periods with a total length of 6000 nm along the x axis is used (see Fig. S3 within the Supplemental Material [38]). From the left and right edges, the meander is extended with homogeneous CoFeB regions of constant thickness d and lengths of 1000 nm. To excite and detect SW excitations, we use regions with a width of 100 nm located at a distance of 800 nm from the edges of the structure. The distance between the centers of the excitation and detection regions is 6100 nm. To avoid the reflection of SWs at the edges of the structure, 700-nm-wide absorbing boundary layers (ABLs) along the x axis are introduced with an increase in the Gilbert damping according to $\alpha(x) = \alpha_0(x - x_0)^2$ (with x_0 the coordinate at the beginning of the ABL) from a minimum value of 0.003 to a maximum of 1 [41].

V. RESULTS AND DISCUSSION

The frequencies of the SW modes are extracted by fitting the peaks in the BLS spectra (displayed in Fig. 2) with Lorentzian functions. The results are plotted as a function of their respective wave vectors (k) up to the fourth BZ in Fig. 3. The magnonic band structure shows periodic branches in the dispersion relation as well as the frequency ranges, in which SWs are forbidden to propagate through the crystals. Note that the overall features of the measured dispersions are quantitatively reproduced well by the micromagnetic simulations (solid lines in Fig. 3).

Let us first analyze the band structure for the 23-12 sample. The amplitude of the magnonic band is more pronounced for the two lowest frequency modes and decreases

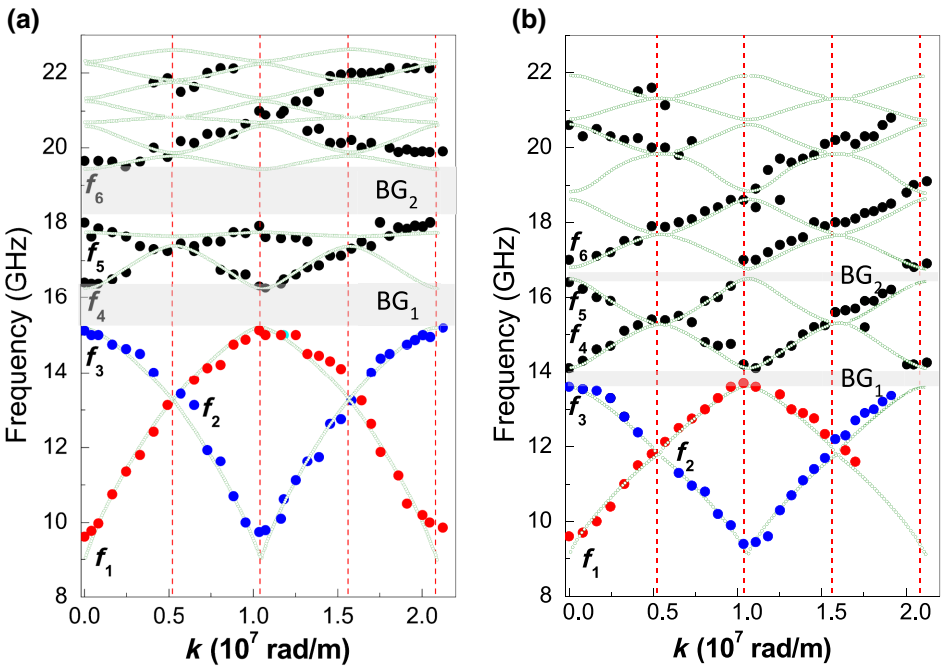

FIG. 3. Measured magnonic band structure for the vertical meander-shaped (a) 23-12 and (b) 15-8 CoFeB films. Red and blue points represent the frequency of the lowest two frequency peaks in Fig. 2 while micromagnetic dispersion data are represented by the green solid lines. The gray regions indicate the BG$_m$ frequency ranges for $m = 1$ and 2.

for the highest ones. The frequencies of this mode doublet oscillate in antiphase within the same frequency range, i.e., from $f_1 = 9.6$ to $f_3 = 15.1$ GHz. Their group velocities $v_g = d\omega/dk$ at $k = 0$ have opposite signs and differ by one order of magnitude, i.e., 7.25×10^3 and -5.23×10^2 m/s for the first- and second-lowest frequency modes, respectively. The resulting magnonic bandwidth of these two modes is f_3-$f_1 = 5.5$ GHz demonstrating a rather large frequency range over which the SWs can propagate along with the vertical meander structure. The third-lowest frequency mode has $v_g = 2.2 \times 10^2$ m/s with a magnonic bandwidth of approximately equal to 1.2 GHz, while the fourth-lowest frequency mode has a much less pronounced dispersive character. Between each successive doublet of modes, full magnonic BGs are observed, where SWs are forbidden to propagate through the crystals. These are highlighted by the gray areas in Fig. 3.

The width of the first BG_1 is 1.05 GHz while that of BG_2 is 1.65 GHz. We notice that, for higher-order modes, BGs are neither observed in the experiment nor predicted by the numerical calculation. Furthermore, no magnonic BG is observed between the two lowest frequency modes for $k = \pi/a = 0.52 \times 10^7$ rad/m. The two lowest frequency modes (red and blues peaks of Fig. 2) merge into one single peak at frequency f_2 with nonvanishing group velocity. This is different from what is generally observed for single- [42] and multilayer [23] 1D MCs where magnons with wavelengths satisfying the Bragg condition $k = \pi/a$ are resonantly scattered back, leading to the formation of BGs in the SW spectra.

A similar frequency dispersion is measured for the 15-8 meander-shaped film, as well with an overall magnonic band shifted downward but exhibiting the same value of the bottom frequency at $k = 0$ (9.6 GHz). The two lowest frequency modes have an oscillation amplitude (4.4 GHz) between 9.6 and 14 GHz, which is smaller compared to the 23-12 sample (5.5 GHz). It is worthwhile to remark that the center frequency position of the band gaps (BG_1 and BG_2) is downshifted and narrower than those observed in the 23-12 sample.

Using micromagnetic simulations, we calculate the spatial profiles of the modes at the edges of the forbidden zones BG_1 (f_3 and f_4) and BG_2 (f_5 and f_6). Magnetic parameters, i.e., the saturation magnetization $M_s = 1400$ kA/m and the exchange constant of $A_{ex} = 2.1 \times 10^{-11}$ J/m, are extracted from measurements of the frequency dispersion of SWs in planar films with thicknesses of 23 and 15 nm (see Fig. S2 within the Supplemental Material [38]). Figure 4 shows the normalized y component of the dynamic magnetization (M_y/M_s) for sample 23-12. Similar results are also obtained for the 15-8 sample. Since the unit cell exhibits mirror symmetry with respect to the vertical y axis, spatial distributions for standing SWs and Bloch waves in the primitive cell will also have a similar type of symmetry. In particular, the modes at frequencies f_3 and

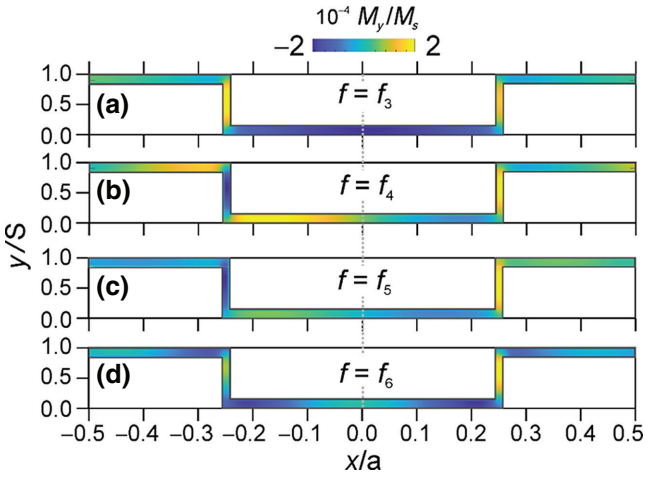

FIG. 4. Spatial distribution of modes (M_y/M_s) in the meander-shaped 23-12 CoFeB film calculated by micromagnetic simulations at the edges of BG_1 (f_3 and f_4) and BG_2 (f_5 and f_6).

f_4, which represent the edges of the first forbidden zone BG_1 in Fig. 3 are symmetric and antisymmetric, respectively, with respect to the center of the meander-shaped film $x = 0$. In contrast, modes f_5 and f_6 for BG_2 are antisymmetric and symmetric with respect to $x = 0$. The mode profiles of Fig. 4 are also plotted in Fig. S4 within the Supplemental Material [38] as a function of the meander coordinate ξ. These observations suggest that the mode profiles at the BG edges correspond to standing waves with zero group velocity and the same Bloch wave number $k = 2\pi m/a,\ m = \pm 1, \pm 2 \ldots$. in a periodic meander structure. These stationary waves are formed by successive reflections of propagative waves when the Bragg condition is fulfilled. Symmetric mode profiles alternate with the antisymmetric ones along with monotonous frequency increase at $k = 2\pi m/a,\ m = \pm 1, \pm 2 \ldots$., while at $k = \pi n/a,\ n = \pm 1, \pm 2 \ldots$. the mode profile is subjected to a smooth transition from the top of one opened BG to the bottom of the next-order BG.

To understand in more detail the formation of the magnonic BGs in these samples, we use the TMM, a standard approach [25,26,43], to study the wave-propagation characteristics in photonic [44], magnonic [45–47], and phononic [48] crystal waveguides and to analyze in detail the calculated frequency dispersion of all modes and their spatial profiles. We assume a meander-shaped film, which is infinite along the z axis while being characterized along the x axis by a period a. Along the y axis the structure has a depth S. For $\mu_0 H$ applied along the z direction, MSSWs propagate at a certain frequency in the horizontal and vertical segments of a unit cell of thickness d_1 and width d_2 since the wave numbers k_1 and k_2, are perpendicular to the direction of the externally applied field, as shown in Fig. 1(a). The exchange interaction as well as

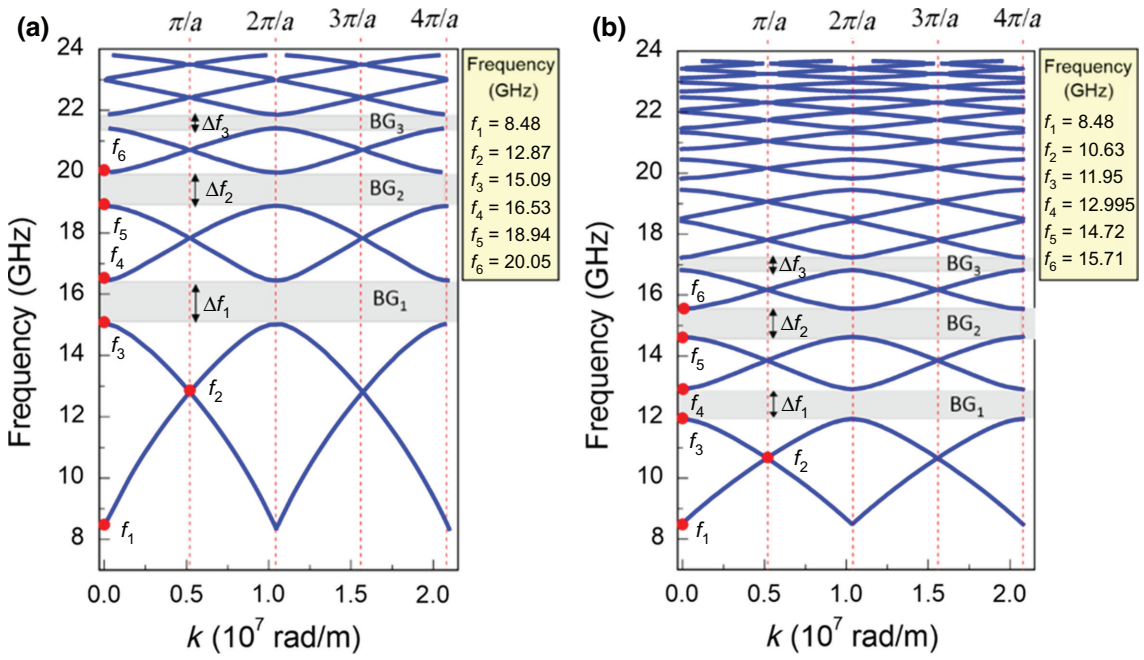

FIG. 5. (a) Dispersion diagram of dipolar SWs in a meander-type structure with thicknesses $d_1 = 23$ and $d_2 = 12$ nm. The position and the width of the first three forbidden zones (BG_{1-3}, Δf_{1-3}) are depicted. The dashed lines indicate the values of the Bloch wave numbers $k_m = m\pi/a$. The characteristic frequencies f_{1-6} are denoted with red dots. (b) As in (a) for $d_1 = 15$ nm and $d_2 = 8$ nm.

a possible magnetic anisotropy are neglected in the calculations. The periodicity of the structure is introduced by cascading the meander-shaped periods and considering the SW amplitude at the input (Ψ_n at $x = -a/2$) and output (Ψ_{n+1} at $x = +a/2$) of each period as determined by interference effects between the incident, reflected, and transmitted SWs. The general dispersion equation connecting the Bloch wave number k with the frequency ω and wave numbers k_1 and k_2 of SWs has a simple form:

$$ka = \arccos(\Phi) + 2\pi m, \quad m = 0, \pm 1, \pm 2 \ldots . \qquad (1)$$

where

$$\Phi = \frac{\Gamma^4 \cos(\chi - \delta) + 2\Gamma^2[1 - \cos(\delta) - \cos(\chi)] + \cos(\chi + \delta)}{(\Gamma + 1)^2(\Gamma - 1)^2},$$

$\delta = 2k_2(\omega)(S - d_1)$ and $\chi = 2k_1(\omega)L_1$. $\Gamma = (d_1 - d_2)/(d_1 + d_2)$ defines the reflection coefficient from the junction of two waveguides in the case of the wave propagating in the section with larger thickness and then traveling along the section with smaller thickness.

For MSSWs propagating in the meander-shaped film, the dispersion equation has a simple form:

$$k_{1,2}(\omega) = -\frac{1}{2d_{1,2}} \ln\left\{1 - \frac{4[\omega^2 - \omega_h(\omega_h + \omega_m)]}{{\omega_m}^2}\right\}, \qquad (2)$$

where $\omega_h = \gamma H_0, \omega_m = \gamma \mu_0 M_s$, and γ is the gyromagnetic ratio, M_s is the saturation magnetization. Further details of the TMM are described within the Supplemental Material [38].

Figures 5(a) and 5(b) show the result of SW band-structure calculations performed using Eqs. (S10) and (S11) for the two meander-shaped CoFeB films (23-12 and 15-8) for an external magnetic field $\mu_0 H_0 = 50$ mT applied along the z axis, as shown in Fig. 1(a). The calculated band structures exhibit similar features: all modes have an oscillating frequency behavior with the same periodicity and BG width (Δf), which decreases monotonically with increasing mode frequency ($BG_1 > BG_2 > BG_3$). The magnonic bandwidth and BG for the 23-12 sample are larger than for the 15-8 sample, which, by contrast, exhibits a larger number of modes in the same frequency range.

In addition, when comparing the results in Fig. 5(a) to those calculated by micromagnetic simulations in Fig. 3(a) for sample 23-12, we notice that the two approaches provide similar results for the dispersion of the lowest three modes while for the fourth-lowest frequency mode micromagnetic calculations provide an almost constant frequency value. Moreover, the TMM predicts that the width of the BGs decreases for increasing mode frequency, whereas this is not the case for the micromagnetic band structure, as shown in Fig. 3. These discrepancies are mainly ascribed to the fact that intralayer exchange interaction is neglected in the TMM calculations.

The results of the TMM numerical calculations for the spatial distribution of $|\Psi|$ along the coordinate ξ at frequencies from f_1 to f_6 are shown in Figs. 6(a)–6(c) for the

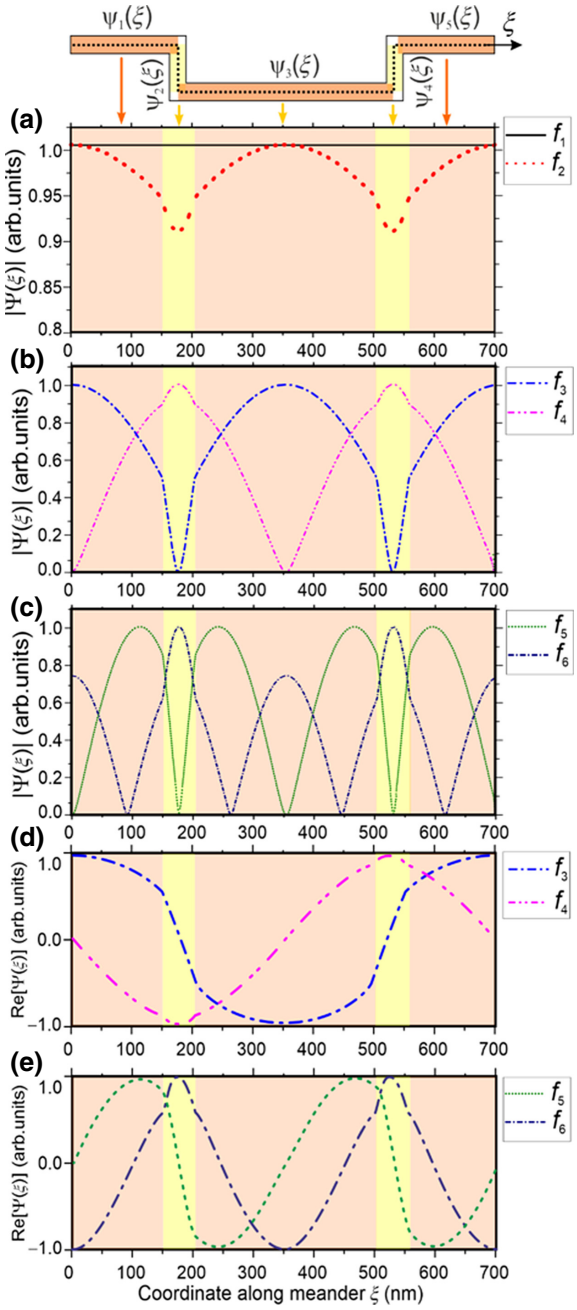

FIG. 6. (a)−(c) Scheme for setting the eigenfunction form along the corresponding segments of the structure with coordinate ξ together with the absolute value of the spatial SW mode amplitudes (Ψ) at different frequencies from f_1 to f_6. Notice that in (a) the vertical scale for $|\Psi(\xi)|$ goes from 0.8 to 1 and not from 0 to 1 like in (b) and (c). (d) Real part of spatial distribution of SW amplitudes at frequencies f_3, f_4 demonstrating the localization either in vertical or in horizontal segments and symmetry with respect to the center of the unit cell ($x = 0$). (e) As in (d) for modes at frequencies f_5 and f_6.

23-12 sample. The lowest-frequency mode at frequency f_1 is uniformly distributed along the meander-shaped CoFeB film and resembles the Kittel mode of ferromagnetic resonance. Mode f_2 has a similar profile as f_1 but presents a shallow minimum in the vertical segment. The dispersion characteristics in the vicinity of f_2 show two passbands connecting at a point $2kL_1 = \pi a$ and corresponding to symmetric and antisymmetric modes with respect to the yz-plane crossing $x = 0$ position. At $2kL_1 > \pi$, the symmetric mode becomes antisymmetric and vice versa. It should be noted that the dispersion characteristics of waves in periodic structures are determined not only by the material parameters of the media and the geometry of the unit cells but also by their symmetry.

The CoFeB−based meander structure studied in this paper show a mirror symmetry with respect to the y-z plane passing through the point $x = 0$ and a gliding plane symmetry (glide reflection symmetry). A unit cell of a meander structure [Fig. 1(a)] can be obtained from a part of a cell of length $a/2$ by performing two operations: reflection relative to a plane parallel to the coordinate plane (x, z) and passing through the point $y = S/2$ and translation along the x axis by a distance of $a/2$. A similar type of symmetry can be found in microstrip meander-line slow-wave structures (MMLSWS), which are widely used in microwave and rf vacuum electronic power sources [29,30]. In Refs. [31,32], the dispersion characteristics of electromagnetic waves in MMLSWS, mode symmetry, and forbidden bands have been analyzed by the Green function method in the quasitransversal electromagnetic wave approximation. In particular, it was shown that the normal modes of MMLSWS are even and odd modes with respect to the mirror plane of symmetry. Thus, in the frequency region where $k = (m\pi/a)$, $m = 1, 3, 5\ldots$ the band gaps are absent in contrast to one-dimensional planar magnonic crystal [49]. Band gaps are observed only at $k = (m2\pi/a)$, $m = 1, 2, 3\ldots$ Consequently, the periodicity of the frequency oscillation is $4\pi/a$ and not $2\pi/a$. Similar considerations hold for the 15-8 meander-shaped film.

At the frequency f_3, the global minimum of the spatial distribution ($|\Psi(x)|$) is localized in the vertical segments, while global maxima are localized in the horizontal segments [see Fig. 6(b)]. At frequency f_4, the distribution changes to the opposite. Notice that the modes at frequencies f_3 and f_4 correspond to the bottom (f_{b1}) and top (f_{t1}) frequencies of the BG_1. A similar variation in the spatial distribution in the vertical segments during the transition from f_3 to f_4 is also observed at the edges of the $BG_{2,3}$ zones. Figure 6(c) shows the spatial profiles of modes f_5 and f_6, which correspond to the bottom (f_{b1}) and top (f_{t1}) frequency for BG_2. Figures 6(d) and 6(e) show the real part of the SW amplitude for modes f_3-f_4 and f_5-f_6, respectively. At the frequency $f_{b1} = f_3$, the function $\Psi(x)$ is symmetric with respect to $x = 0$ while at frequency $f_{t1} = f_4$, it is antisymmetric. Contrarily, for mode $f_{b2} = f_5$ the real part of the function $\Psi(x)$ is antisymmetric with respect to $x = 0$ while for $f_{t2} = f_6$ it is symmetric. These findings are in agreement

with the results of micromagnetic calculations in Fig. 4.

To obtain further insight into the magnonic band structure and the SW transmission in the nanoscale meander-shaped film, we analytically analyze the dependence of the BG width (Δf_m) and the center frequencies f_{cm} for the different modes with numbers $m = 1, 2, 3$ on the width d_2 of the magnetic vertical segment at fixed values of $d_1 = 23$ nm and $h = 50$ nm. In the TMM, it is assumed that the internal magnetic field in all segments of the meander structure is uniform and the SW reflection coefficients $\Gamma = (d_1 - d_2)/(d_1 + d_2)$ are determined only by the ratios of the thicknesses and the width of the horizontal and vertical segments, respectively.

The first observation that can be derived from Fig. 7(a) is that the BG_m width is not monotonic as a function of d_2 in the range between 1 and 40 nm. When $d_2 > d_1$, there is no significant difference between the BG_m width for the different modes. We find that when $d_2 = d_1 = 23$ nm the SW reflection coefficient in the meander structure is $\Gamma = 0$ and therefore SWs propagate without reflection at the joints of segments, i.e., the forbidden zones for all the modes disappear. This indicates that the SWs can be transferred between different lavers of a 3D nanostructure without significant loses, enabling thus 3D routing for SWs. For $d_2 < d_1$, the propagation constant of the SWs, k_2, in the vertical segments increases, since for any frequency ω, it follows from the dispersion equation [Eq. (11) within the Supplemental Material [38]] that $k_2(\omega) = (d_1/d_2)k_1(\omega)$ ($\Gamma > 0$) and an almost linear increase in the BG width is observed. The zone with the number $m = 1$ has the largest Δf_m, which decreases for increasing band-gap order m. Upon further reduction of d_2, the BG_1 width increases, reaching a maximum at $d_2 = 3.5$ nm, and then vanishing for d_2 approaching zero. By contrast, BG_2 and BG_3, show an oscillating behavior with minima and maxima, whose positions depends on m. This means that by choosing the width d_2 of the vertical segments, one can selectively control the width and center frequencies of the forbidden zones with different indices m. From the dependency $\Delta f_m(d_2)$ [see Fig. 7(a)], we define the corresponding zone center frequencies $f_{cm}^j(d_{2m}^j)$, which exhibit a monotonic increase up to about 7.5 nm followed by an almost constant value for larger d_2 width [Fig. 7(b)].

We also calculate the dependence of the BG_m width Δf_m [Fig. 7(c)] and the center frequencies f_{cm} of the forbidden zones [Fig. 7(d)] with numbers $m = 1,2,3$ as a function of the meander depth h in the range between 37 and 177 nm. The results show that the dependence of the width Δf_m for

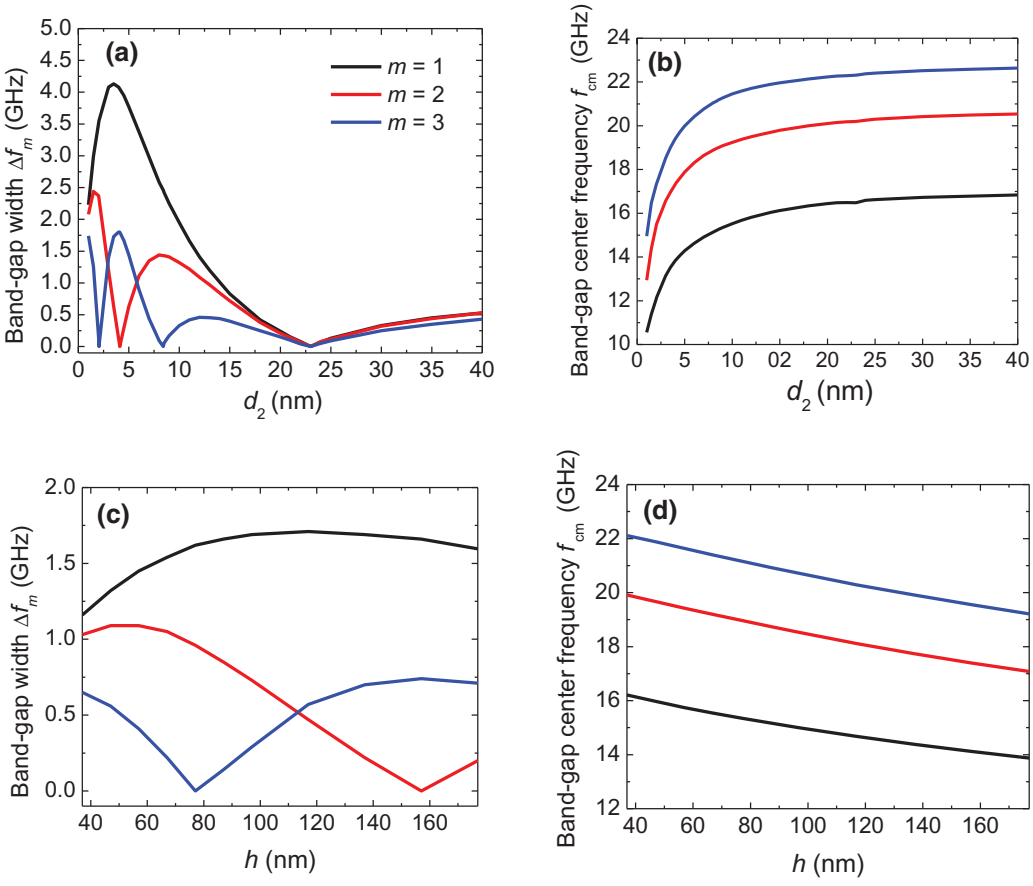

FIG. 7. (a) Dependence of the BG width (Δf_m) and (b) center frequencies f_{cm} on the width of the vertical segment d_2 of the meander-shaped film with $d_1 = 23$ nm. (c) BG width (Δf_m) and (d) center frequencies f_{cm} as a function of the meander depth h with $d_1 = 23$ nm and $d_2 = 12$ nm. Data are shown for the three lowest frequencies BG_m ($m = 1,2$, and 3).

increasing meander depth h is nonmonotonous. In particular, at certain values of h, the BG dispersion characteristics of SWs vanish for $m = 2$ and $m = 3$. On increasing h, the central frequencies of the forbidden zones f_{cm} decrease monotonously. Similar considerations hold for the 15-8 sample (see Fig. S5 within the Supplemental Material [38]) even if the BG width vanishes at different d_2 and h values with respect to the 23-12 sample. Thus, by a careful choice of the meander-height h, one can selectively control the width and center frequencies of the forbidden zones with different indices m, and thus tune the SW transmission in such 3D nanostructures.

VI. SUMMARY

In summary, using wavevector-resolved Brillouin-light-scattering spectroscopy, micromagnetic simulations, and analytical models we analyze the propagation characteristics of spin waves in vertical meander-shaped $Co_{40}Fe_{40}B_{20}$ films formed by nanosegments at 90° with respect to each other. We determine the dispersion relations and reveal the periodic character of the different dispersive branches as well as the frequency ranges where spin waves are allowed or forbidden to propagate. Furthermore, the characteristics of the magnonic band structure can be effectively controlled by changing the geometric parameters of the vertical nonsegments allowing the magnonic band structure to be engineered.

Micromagnetic simulations and analytical calculations have allowed us to understand and explain the formation of the magnonic band gaps in terms of the mode spatial localization and symmetry. We show that the spatial distribution of the modes for frequencies at the lower edge of the band gap have symmetric distribution with respect to the unit cell of the meander structure, whereas for the upper bound frequencies they have an asymmetric distribution. This is in very good agreement with the electromagnetic energy density distribution at the edges of the forbidden zones in 1D photonic crystals, thus demonstrating the spin-wave propagation in nanoscale magnetic structures. The results show that the investigated structures behave as three-dimensional spin-wave waveguides enabling thus the vertical spin-wave transport. Such 3D nanostructures thus form a key step towards multilevel magnonic architectures for signal processing.

ACKNOWLEDGMENT

This work is partially funded by IMEC's industrial affiliate program on beyond-CMOS logic as well as by the European Union's Horizon 2020 research and innovation program within the FET-OPEN project CHIRON under Grant Agreement No. 801055. The numerical simulation and theoretical model for three-dimensional magnonic band structure is supported by Russian Science Foundation (Project No. 20-79-10191). E.B. acknowledges the support from Russian Ministry of Education and Science (Project No. FSRR-2020-0005) and RFBR (Project No.19-29-03034). S.N. acknowledges support by Russian Science Foundation (Project No. 19-19-00607) and Russian Federation State support (project no. 075-15-2019-1874).

[1] J. Vasseur, L. Dobrzynski, B. Djafari-Rouhani, and H. Puszkarski, Magnon band structure of periodic composites, Phys. Rev. B **54**, 1043 (1996).

[2] S. A. Nikitov, Ph. Tailhades, and C. S. Tsai, Spin waves in periodic magnetic structures-magnonic crystals, J. Magn. Magn. Mater. **236**, 320 (2001).

[3] H. Puszkarski and M. Krawczyk, Magnonic crystals- the magnetic counterpart of photonic crystals, Solid State Phenomena **94**, 125 (2003). (Trans Tech Publ).

[4] J. Topp, D. Heitmann, M. P. Kostylev, and D. Grundler, Making a Reconfigurable Artificial Crystal by Ordering Bistable Magnetic Nanowires, Phys. Rev. Lett. **104**, 207205 (2010).

[5] M. Vogel, A. V. Chumak, E. H. Waller, T. Langner, V. Vasyuchka, B. Hillebrands, and G. von Freymann, Optically reconfigurable magnetic materials, Nat. Phys. **11**, 487 (2015).

[6] P. A. Kolodin and B. Hillebrands, Spin-wave propagation across periodically corrugated thin metallic ferromagnetic films, J. Magn. Magn. Mater. **161**, 199 (1996).

[7] S. Tacchi, F. Montoncello, M. Madami, G. Gubbiotti, G. Carlotti, L. Giovannini, R. Zivieri, F. Nizzoli, S. Jain, A. O. Adeyeye, and N. Singh, Band Diagram of Spin Waves in a Two-Dimensional Magnonic Crystal, Phys. Rev. Lett. **107**, 127204 (2011).

[8] G. Gubbiotti, S. Tacchi, M. Madami, G. Carlotti, S. Jain, A. O. Adeyeye, and M. P. Kostylev, Collective spin waves in a bicomponent two-dimensional magnonic crystal, App. Phys. Lett. **100**, 162407 (2012).

[9] D. Kumar, J. W. Klos, M. Krawczyk, and A. Barman, Magnonic band structure, complete bandgap and collective spin wave excitation in nanoscale two-dimensional magnonic crystals, J. Appl. Phys. **115**, 043917 (2014).

[10] M. Krawczyk and D. Grundler, Review and prospects of magnonic crystals and devices with reprogrammable band structure, J. Phys.: Condens. Matter **26**, 123202 (2014).

[11] A. V. Chumak, A. A. Serga, and B. Hillebrands, Magnonic crystals for data processing, J. Phys. D: Appl. Phys. **50**, 244001 (2017).

[12] S. Tacchi, P. Gruszecki, M. Madami, G. Carlotti, J. W. Klos, M. Krawczyk, A. Adeyeye, and G. Gubbiotti, Universal dependence of the spin wave band structure on the geometrical characteristics of two-dimensional magnonic crystals, Sci. Rep. **5**, 10367 (2017).

[13] K. Zakeri, Magnonic crystals: Towards terahertz frequencies, J. Phys.: Condens. Matter **32**, 363001 (2020).

[14] K. Baumgaertl, S. Watanabe, and D. Grundler, Phase control of spin waves based on a magnetic defect in a one-dimensional magnonic crystal, Appl. Phys. Lett. **112**, 142405 (2018).

[15] H. Qin and S. van Dijken, Nanometer-thick YIG-based magnonic crystals: Bandgap dependence on groove depth, lattice constant, and film thickness, Appl. Phys. Lett. **116**, 202403 (2020).

[16] A. Barman, S. Mondal, S. Sahoo, and A. De, Magnetization dynamics of nanoscale magnetic materials: A perspective, J. Appl. Phys. **128**, 170901 (2020).

[17] V. V. Kruglyak, S. O. Demokritov, and D. Grundler, Magnonics, J. Phys. D: Appl. Phys. **43**, 264001 (2010).

[18] G. Csaba, Á Papp, and W. Porod, Perspectives of using spin waves for computing and signal processing, Phys. Lett. A **381**, 1471 (2017).

[19] A. Mahmoud, F. Ciubotaru, F. Vanderveken, A. V. Chumak, S. Hamdioui, C. Adelmann, and S. Cotofana, An introduction to spin wave computing, J. Appl. Phys. **128**, 161101 (2020).

[20] Y. Li, W. Zhang, V. Tyberkevych, W.-K. Kwok, A. Hoffmann, and V. Novosad, Hybrid magnonics: Physics, circuits, and applications for coherent information processing, J. Appl. Phys. **128**, 130902 (2020).

[21] M. Mruczkiewicz, P. Graczyk, P. Lupo, A. Adeyeye, G. Gubbiotti, and M. Krawczyk, Spin-wave nonreciprocity and magnonic band structure in a thin permalloy film induced by dynamical coupling with an array of Ni stripes, Phys. Rev. B **96**, 104411 (2017).

[22] P. Graczyk, M. Krawczyk, S. Dhuey, W.-G. Yang, H. Schmidt, and G. Gubbiotti, Magnonic band gap and mode hybridization in continuous permalloy films induced by vertical dynamic coupling with an array of permalloy ellipses, Phys. Rev. B **98**, 174420 (2018).

[23] G. Gubbiotti, X. Zhou, Z. Haghshenasfard, M. G. Cottam, and A. O. Adeyeye, Reprogrammable magnonic band structure of layered permalloy/Cu/permalloy nanowires, Phys. Rev. B **97**, 134428 (2018).

[24] Q. Wang, P. Pirro, R. Verba, A. Slavin, B. Hillebrands, and A. V. Chumak, Reconfigurable nanoscale spin-wave directional coupler, Sci. Advances **4**, e1701517 (2018).

[25] A. V. Sadovnikov, V. A. Gubanov, S. E. Sheshukova, Yu. P. Sharaevskii, and S. A. Nikitov, Spin-wave Drop Filter Based on Asymmetric Side-Coupled Magnonic Crystals, Phys. Rev. Appl. **9**, 051002 (2018).

[26] A. V. Sadovnikov, A. A. Grachev, V. A. Gubanov, S. A. Odincov, A. A. Martyshkin, S. E. Sheshukova, Yu. P. Sharaevskii, and S. A. Nikitov, Spin-wave intermodal coupling in the interconnection of magnonic units, Appl. Phys. Lett. **112**, 142402 (2018).

[27] M. T. Bohr and I. A. Young, CMOS scaling trends and beyond, IEEE Micro **37**, 20 (2017).

[28] J. P. Colinge, *FinFETs and Other Multi-Gate Transistors* (Springer, Boston, MA, 2008).

[29] P. A. Popov, A. Yu. Sharaevskaya, E. N. Beginin, A. V. Sadovnikov, A. I. Stognij, D. V. Kalyabin, and S. A. Nikitov, Spin wave propagation in three-dimensional magnonic crystals and coupled structures, J. Magn. Magn. Mater. **476**, 423 (2017).

[30] A. A. Martyshkin, E. N. Beginin, A. I. Stognij, S. A. Nikitov, and A. V. Sadovnikov, Vertical spin-wave transport in magnonic waveguides with broken translation symmetry, IEEE Trans. Magn. **10**, 5511105 (2019).

[31] G. Gubbiotti, *Three-Dimensional Magnonics* (Jenny Stanford, Singapore, 2019).

[32] K. Szulc, P. Graczyk, M. Mruczkiewicz, G. Gubbiotti, and M. Krawczyk, Spin-Wave Diode and Circulator Based on Unidirectional Coupling, Phys. Rev. Appl. **14**, 034063 (2020).

[33] R. A. Gallardo, D. Cortés-Ortuño, T. Schneider, A. Roldán-Molina, F. Ma, R. E. Troncoso, K. Lenz, H. Fangohr, J. Lindner, and P. Landeros, Flat Bands, Indirect Gaps, and Unconventional Spin-Wave Behavior Induced by a Periodic Dzyaloshinskii-Moriya Interaction, Phys. Rev. Lett. **122**, 067204 (2019).

[34] J. A. Otálora, M. Yan, H. Schultheiss, R. Hertel, and A. Kákay, Curvature-induced Asymmetric Spin-Wave Dispersion, Phys. Rev. Lett. **117**, 227203 (2016).

[35] K. Vogt, F. Y. Fradin, J. E. Pearson, T. Sebastian, S. D. Bader, B. Hillebrands, A. Hoffmann, and H. Schultheiss, Realization of a spin-wave multiplexer, Nat. Commun. **5**, 3727 (2014).

[36] J. Stigloher, M. Decker, H. S. Körner, K. Tanabe, T. Moriyama, T. Taniguchi, H. Hata, M. Madami, G. Gubbiotti, K. Kobayashi, T. Ono, and C. H. Back, Snell's law for Spin Waves, Phys. Rev. Lett. **117**, 037204 (2016).

[37] G. Carlotti and G. Gubbiotti, Magnetic properties of layered nanostructures studied by means of brillouin light scattering and the surface magneto-optical Kerr effect, J. Phys.: Condens. Matter **14**, 8199 (2002).

[38] See Supplemental Material at http://link.aps.org/supplemental/10.1103/PhysRevApplied.15.014061 for the Magneto-optic Kerr effect loops (Fig. S1); Measured and calculated spin-wave dispersion for the 23 and 15 nm thick plane CoFeB films(Fig. S2); Details of the micromagnetic simulations (Fig. S3); Calculated spatial profiles at the modes at the edges of the first (BG1) and second (BG2) bang gaps (Fig. S4); Transmission matrix method for magnonic band structure and mode profiles calculations; Dependences of the BG width and center frequencies (b) on the width of the vertical segment d_2 of the meander-shaped film with $d_1 = 15$ nm (Fig. S5).

[39] J. R. Sandercock, in *Light Scattering in Solids III*, edited by M. Cardona, G. Guntherodt (Springer Series in Topics in Applied Physics Vol. 51, Springer-Verlag, Berlin, 1982), pp. 173.

[40] A. Vansteenkiste, J. Leliaert, M. Dvornik, M. Helsen, F. Garcia-Sanchez, and B. Van Waeyenberge, The design and verification of mumax3, AIP Advances **4**, 107133 (2014).

[41] G. Venkat, H. Fangohr, and A. Prabhakar, Absorbing boundary layers for spin wave micromagnetics, J. Magn. Magn. Mater. **450**, 34 (2018).

[42] G. Gubbiotti, S. Tacchi, G. Carlotti, N. Singh, S. Goolaup, A. O. Adeyeye, and M. P. Kostylev, Collective spin modes in monodimensional magnonic crystals consisting of dipolarly coupled nanowires, Appl. Phys. Lett. **90**, 092503 (2007).

[43] A. V. Sadovnikov, A. A. Grachev, S. E. Sheshukova, Yu. P. Sharaevskii, A. A. Serdobintsev, D. M. Mitin, and S. A. Nikitov, Magnon Straintronics: Reconfigurable Spin-Wave Routing in Strain-Controlled Bilateral Magnetic Stripes, Phys. Rev. Lett. **120**, 257203 (2018).

[44] J. D. Joannopoulos, S. G. Johnson, J. N. Winn, and R. D. Meade, *Photonic Crystals Molding the Flow of Light*, 2nd edn (Princeton University Press, Princeton, New Jersey, 08540, 44, 2008).

[45] R. Carter, in *Microwave and RF Vacuum Electronic Power Sources* (The Cambridge RF and Microwave Engineering Series, Cambridge University Press, Cambridge, 2018), pp. 134.

[46] K. Wu, *Slow Wave Structures* (Wiley Encyclopedia of Electrical and Electronics Engineering, John Wiley & Sons, 1999).

[47] J. A. Weiss, Dispersion and field analysis of a microstrip meander-ine slow-wave structure, IEEE Trans. Microw. Theory Tech. **22**, 1194 (1974).

[48] R. Crampagne and M. Ahmadpanah, Meander and interdigital lines as periodic slow-wave structures. Part I. Characteristics of waves propagating along an infinite array, Int. J. Electron. **43**, 19 (1977).

[49] Z. K. Wang, Z. V. L. Zhang, H. S. Lim, S. C. Ng, M. H. Kuok, S. Jain, and A. O. Adeyeye, Observation of frequency band gaps in a one-dimensional nanostructured magnonic crystal, Appl. Phys. Lett. **94**, 083112 (2009).